Computational Study on Aerodynamic Mitigation of Wind-Induced, Large-Amplitude Vibrations of Stay Cables with Strakes

DongHun Yeo [a*], Nicholas P. Jones [b]

[a] *National Institute of Standards and Technology, Gaithersburg, MD, U.S.A., donghun.yeo@nist.gov*
[b] *Johns Hopkins University, Baltimore, MD, U.S.A., npjones@jhu.edu*

ABSTRACT

Modifications of circular cylinder surfaces, such as strakes and helical wires, effectively mitigate Kármán vortex-induced vibrations normal to flow and have been applied to the reduction of large-amplitude vibrations of stay cables in bridges, which occur under wind oblique to a cable with or without rainfall. This aerodynamic control method cannot be fully effective without understanding the behavior of the flow around and the associated forces on oblique cables. To address this issue, flow around a yawed cylinder with various strake patterns was studied using three-dimensional detached eddy simulation (DES) at Reynolds number of 1.4×10^5. Results demonstrated that strake patterns strongly influence the development of flow structures around a yawed cylinder and therefore the associated forces on the cylinder. The results suggest that particular strake patterns can mitigate large-amplitude and low-frequency vibrations of stay cables induced by oblique wind.

Keywords: cable vibration, cable-stayed bridge, yawed circular cylinder, detached eddy simulation (DES), strake effect, aerodynamic control.

* Corresponding author. Tel: 1-301-975-8103; fax. 1-301-869-6275.
E-mail address: donghun.yeo@nist.gov (DongHun Yeo)

1 INTRODUCTION

Large-amplitude cable vibrations cause concerns for both the safety and serviceability of cable-stayed bridges. These vibrations have been frequently observed since the first report of vibrations with rain (Hikami and Shiraishi, 1988). They are generally known as "rain-wind induced vibrations" because of their common occurrence with rain, but they have been also observed in the absence of precipitation (Main and Jones, 1999; Matsumoto et al., 1998). These oscillations have much lower frequencies and larger amplitudes than the classical Kármán vortex-induced vibrations in the same wind environment. Their Reynolds numbers (Re) range generally between 0.5×10^5 and 2.0×10^5 (Matsumoto, 1998; Zuo and Jones, 2006).

To mitigate this problem, mechanical and aerodynamic approaches have been proposed and applied to cable-stayed bridges. They require additional investment in constructing and maintaining countermeasures such as dampers. However, such countermeasures cannot be fully effective without understanding the fundamental mechanisms of the wind-induced vibrations. Extensive research has been devoted to investigating factors that contribute to the cable vibrations; however, there remain aspects of the problem that are not yet understood. Excitation mechanisms suggested to date by various researchers can be categorized as high speed vortex-induced vibration and galloping instability. The former is related to a velocity-restricted response (Matsumoto, 1998), and the latter is related to flow instability due to water rivulets (Hikami and Shiraishi, 1988; Verwiebe and Ruscheweyh, 1998) or cable inclination (Larose et al., 2003). However, because the approaches employed in the studies above were two-dimensional or equivalent, they could not account for the three-dimensional characteristics of flow oblique to a very slender cylinder, which are essential to understanding the aerodynamic phenomena associated with the cable vibrations.

Research on flow oblique to a circular cylinder has been conducted for decades. Early theoretical and experimental studies used a quasi-two-dimensional approximation that focuses on the effect of the normal-to-cylinder flow component on flow around a yawed cylinder as the major parameter (Hanson, 1966; King, 1977; Van Atta, 1968). This is known as the independence principle or the cosine rule. However, this quasi-two-dimensional approximation did not clearly indentify the complex three-dimensional flow field oblique to a cylinder. The existence of rotating flow structures that move parallel to the yawed cylinder axis has been observed in experiments (Matsumoto et al., 1990; Shirakashi et al., 1986; Tournier and Py, 1978). Experiments have also reported significant combined effects of the spanwise aspect ratio of the cylinder and the end conditions on the development of flow around a yawed cylinder (Ramberg, 1983).

Three-dimensional numerical studies, by comparison, have enabled to simulate reliably flow oblique to a very slender cylinder using numerical methods such as a periodic boundary condition (Kawamura and Hayashi, 1994; Lucor and Karniadakis, 2003; Yeo and Jones, 2008; Zhao et al., 2009). Yeo and Jones (2008) investigated characteristics of the fully-developed flow around an infinite oblique cylinder at $Re = 1.4\times10^5$ in a 3-D DES, and found that swirling flows with axial and rotational velocity components play an important role in generating complex flow around the cylinder. A sequence of swirling flow structures developed alternatively from both the upper and the lower side of the cylinder and generated multiple local peak forces at approximately equal distances along the cylinder axis. These forces moved along the cylinder at a speed of approximately 90% of the spanwise velocity component of the oncoming flow.

The following mechanism of force generation was suggested by Yeo and Jones (2009). If the von Kármán vortices are strong, as is the case for flow normal to a cylinder (i.e., if the yaw angle is 0 ^{o}), the forces cannot occur. If the yaw angle is beyond a certain limit (e.g., 60 ^{o}), Ká-

rmán vortices do not occur. If the yaw angle is between 0 and 60 º, mitigated strength of Kármán vortex flows occur, and a sequence of swirling flows are generated at low frequency. These flows move along the cylinder as well as exhibiting the features of alternating vorticity shed in the cylinder's wake. The low-frequency components of the moving forces are transmitted along the cylinder axis via modulation of force frequency and amplitude. It is notable that the mitigated Kármán vortices are a necessary condition for the generation of the low-frequency moving forces. Therefore, an aerodynamic countermeasure, such as a modification of the cross section, should be effective when the von Kármán vortices are fully suppressed. A disturbance of the force generation mechanism can be also effective. This understanding of the phenomenon allows the development of aerodynamic approaches that address the *cause* of the vibrations and are thus likely to lead to a more economical and effective mitigation strategy.

For stay cables in cable-stayed bridges, the section modification should be selected to take into account not only the mitigation of the cable vibrations, but also its effect on the aesthetics of the bridge. For these reasons, excessive sectional modifications (e.g., a hemispherical bumped cylinder and a wavy cylinder), have not been considered as a countermeasure for vibrations of stay cables, even though they are effective in reducing the strength of flow-induced force (Choi et al., 2008; Lam et al., 2010; Lam et al., 2004; Wang et al., 2004; Zou and Lin, 2009), Instead, minimal modifications, such as spiral strakes or helical fillets have been suggested and used in past mitigation strategies. However, their deployment has generally not been based on analytical/computational studies or rational design procedures (Kleissl and Georgakis, 2010; Matsumoto, 1998; Miyata et al., 1994; Phelan et al., 2006). Only for the case of a cylinder normal to flow have aerodynamic effects of strakes on the cylinder been studied intensively. According to (Zdravkovich, 1981), the use of helical strakes was reported to be an effective method

of attenuating vortex shedding from a circular cylinder when the flow is normal to the cylinder. Experimental results showed that three or four helical wires with approximately 0.1*D* diameter are most effective at a pitch between 10*D* and 14*D*, where *D* is a diameter of the cylinder (Weaver, 1961). Recently numerical studies have been performed as well (Pinto et al., 2006; Pontaza et al., 2009). (Note, however, that according to Ruscheweyh (1994) the effectiveness of the strakes is weak if the Scruton number is less than about 8.)

The goal of this study was to propose the development of an approach that uses a suitably defined strake pattern to effectively disturb three-dimensional flow structures that generate the low-frequency forces. This paper focuses on understanding the effect of strake patterns on the three-dimensional characteristics of the flow around a yawed circular cylinder and on the reduction of the associated forces causing large-amplitude cable vibrations.

2 NUMERICAL SIMULATION

Three-dimensional simulations with the Spalart-Allmaras DES model were conducted for a flow past a 40°-yawed cylinder of 10*D* length with strakes at Re = 1.4×10^5 (based on freestream velocity *U* and the diameter of the cylinder *D*). The computations were performed using the Wind-US CFD 1.0 (Computational Fluid Dynamics) code based on a cell-vertexed finite-volume approach (Wind-US, 2009). The code has been developed and maintained by the NPARC (National Project for Application-oriented Research in CFD) Alliance.

2.1 *Spalart-Allmaras DES approach*

Detached eddy simulation (DES), developed by Spalart et al. (1997), is a hybrid approach to turbulence modeling by large eddy simulation (LES) and Reynolds averaged Navier-Stokes simulation (RANS). The Spalart-Allmaras (S-A) DES approach employs a conventional RANS ap-

proach in the boundary layers near a wall, but uses an LES-like approach in the separated flow away from a wall by modifying the RANS turbulence model (Spalart and Allmaras, 1992).

The S-A DES employs a DES length scale $\tilde{d}$ instead of distance to the closest wall d from the standard S-A model. The new length scale is defined as:

$$\tilde{d} \equiv \min(d, C_{\mathrm{DES}}\Delta) \tag{1}$$

where Δ, defined by $\Delta = \max(\Delta x, \Delta y, \Delta z)$, is the maximum grid spacing in the three-dimensional structured grid cell, and the adjustable constant C_{DES} is recommended as 0.65 for homogeneous turbulence by Shur et al. (1999). The model functions as a RANS model where $\tilde{d} = d$, and works as a subgrid-scale model where $\tilde{d} = C_{\mathrm{DES}}\Delta$. Therefore, the behavior of the model is controlled by grid spacing.

The turbulent viscosity equation of the S-A model is

$$\frac{D\tilde{\nu}}{Dt} = c_{b1}\tilde{S}\tilde{\nu} + \frac{1}{\sigma}\left\{\nabla\cdot\left[(\nu+\tilde{\nu})\nabla\tilde{\nu}\right] + c_{b2}(\nabla\tilde{\nu})^2\right\} - c_{w1}f_w\left[\frac{\tilde{\nu}}{\tilde{d}}\right]^2 \tag{2}$$

From the above equation the turbulent kinematic viscosity is determined by

$$\nu_T = \frac{\mu_T}{\rho} = \tilde{\nu}f_{v1}, \qquad f_{v1} = \frac{\chi^3}{\chi^3 + c_{v1}^3}, \qquad \chi \equiv \frac{\tilde{\nu}}{\nu} \tag{3}$$

where ν is the molecular viscosity. The modified vorticity $\tilde{S}$, related to the magnitude of vorticity S, is defined as

$$\tilde{S} = S + \frac{\tilde{\nu}}{\kappa^2 d^2} f_{v2}, \qquad f_{v2} = 1 - \frac{\chi}{1+\chi f_{v1}} \tag{4}$$

The wall destruction function f_w is

$$f_w = g\left[\frac{1+c_{w3}^6}{g^6 + c_{w3}^6}\right]^{1/6}, \qquad g = r + c_{w2}(r^6 - r), \qquad r \equiv \frac{\tilde{\nu}}{\tilde{S}\kappa^2 d^2} \tag{5}$$

The closure coefficients are given by

$$
\begin{aligned}
&c_{v1} = 7.1, \qquad c_{b1} = 0.1355, \qquad c_{b2} = 0.622 \\
&\sigma = 2/3, \qquad \kappa = 0.41, \\
&c_{w1} = \frac{c_{b1}}{\kappa^2} + \frac{(1+c_{b2})}{\sigma}, \qquad c_{w2} = 0.3, \qquad c_{w3} = 2.
\end{aligned}
\tag{6}
$$

The first term and the last term in the right-hand side of Eq. (2) are related to production and destruction of turbulent viscosity. When the production and destruction terms in the model are balanced, the length scale $\tilde{d}$ yields a Smagorinsky eddy viscosity and DES acts similarly to LES. This hybrid technique allows unsteady three-dimensional computations at high Reynolds numbers while maintaining manageable computational requirements (Spalart, 2000).

2.2 *Angles and coordinates of a yawed cylinder*

Figure 1 shows a yaw angle, global coordinates of the computational domain, and local coordinates of a yawed cylinder used in this study. The incoming flow goes from left to right. The yaw angle β is defined as the angle from an axis oriented normal to the incoming flow (line AB) to a horizontally skewed cylinder (line AC). The global coordinates consist of the *X* axis in the direction of the incoming flow, *Y* axis in the upward direction normal to the plane ABC, and *Z* axis in the direction normal to the incoming flow (line AB). The local coordinates have an *x* axis in the direction normal to cylinder axis on the plane ABC, *y* axis identical to the *Y* axis, and *z* axis in the direction of the cylinder axis. The global axes are useful to describe information on the incoming flow, and the local coordinates are important for explaining behavior of the flow around and forces on the yawed cylinder.

2.3 *Strake patterns*

Strakes are fitted onto a bare circular cylinder whose diameter is D. Figure 2 depicts the strake patterns on the cylinder investigated in this study. Note that a 20D cylinder is plotted in the figure for illustration purpose, but that a 10D cylinder is used in the simulations. A cylinder of type A has three-start helical strakes of a 10D pitch with 0.1D thickness. The type A pattern was first investigated in this study because it is known as one of most effective patterns to attenuate vortex shedding, as confirmed by Weaver (1961). A cylinder of type B has 12 axial strakes (i.e., 30 ^{o} equiangular intervals) with 0.05D thickness, similar to patterns used in Matsumoto's experiments (1992). Two patterns of Type B were investigated in this study according to strake alignment relative to flow direction (Fig. 3). Type B-1 strakes are aligned symmetrically about the flow direction passing the cylinder center, and Type B-2 strakes are asymmetric to the flow direction as shown in the figure. A type C cylinder has two helical strake patterns; both have 10D pitches and 0.1D thickness, but their rotation directions are opposite along the cylinder axis. This pattern was designed in this study in order to avoid asymmetric separation lines of vortex flows from both sides of the cylinder, regardless of any oblique flow direction.

This study concerns a cylinder with spanwise length 10D and strakes with 10D pitch. The 10D length with periodic spanwise boundary conditions is sufficient to generate the full three-dimensional flow structure that would develop around an infinite cylinder; that structure would consist of a series of swirling flows, each with a 10D length, moving along the cylinder (Yeo and Jones, 2008). The 10D pitch is consistent with the assumed periodic boundary conditions of the 10D long cylinder.

2.4 *Numerical methods*

The computational domain used in the study was taken sufficiently large to minimize unwanted effects of the flow due to location of boundaries and to relative size of the cylinder. As shown in Figure 4(a), the domain had the shape of a parallelepiped whose upstream and downstream boundary walls are skewed (with yaw angle β) from the plane normal to the incoming flow direction, and had an extent of 35D in the streamwise direction (15D in the upstream region and 20D in the downstream region), 25D in the cross-stream direction (12.5D from the center of the cylinder to the top and bottom side), and 10D along the cylinder length in the spanwise direction (i.e., the local z axis).

The simulation imposed a constant velocity for the upstream boundary; the Null Neumann condition for the downstream boundary, except that the static pressure was fixed; slip wall conditions for the top and bottom boundaries; and periodic boundary conditions for both spanwise wall boundaries. A no-slip condition was used without any wall functions on the wall of the cylinder, and sufficient grids were assigned in the viscous layer to directly resolve the boundary layer flow. The first grid normal to the wall in this study is positioned at a distance of $8\times10^{-5}D$ from the wall, whose wall unit of Δy^+ is less than or equal to unity. This non-dimensional viscous length scale is based on the viscosity ν and wall shear stress τ_w of the flow, and is described as

$$y^+ = \sqrt{\frac{|\tau_w|}{\rho}}\frac{y}{\nu} \tag{7}$$

where ρ is the density of the fluid, and y is the distance from the wall.

The total number of grid elements was approximately 1.2×10^6. The simulation used 128 nodes on the cylinder surface along the perimeter and 61 nodes of 0.167D interval along the cyl-

inder length (Fig. 4(b)). The spacing ratio of adjacent grids is less than 1.2 in order to avoid a sudden change of grid sizes. The hyperbolic tangent distribution function with specified ends was applied to distributing the nodes along the grid line for smooth grid generation. Figure 4 shows both grids of a computational domain and of a cylinder with three-start helical strakes in the domain.

The numerical schemes were a fifth order upwind scheme for convection, a second order central scheme for viscosity, and a two-step MacCormack implicit scheme for time integration with four Newton sub-iterations at each timestep. A non-dimensional timestep of 0.01 (calculated as $\Delta t^* = U\Delta t / D$ where Δt is a timestep in dimension) was used.

The simulation assumed turbulent separation from the cylinder surface due to its turbulent boundary layer generated by the S-A DES model. The characteristics of aerodynamic pressures and forces induced by the turbulent separation in this DES study are in good agreement to those by the upstream incoming flow with moderate level of turbulence intensity. Details of verification of numerical parameters, such as grid refinement, timestep, sub-iteration per timestep in the iteration method, order of schemes for convective terms, and validation of the numerical results used in the study are presented in the Appendix.

3 RESULTS OF SIMULATIONS

3.1 *Vortex structures*

Figure 5 shows vortex flow structures past a yawed cylinder (flow from left to right) using an iso-surfaces of the second invariant Q of velocity gradient tensor $u_{i,j}$ (Hunt et al., 1988):

$$Q = \frac{1}{2}\left(\Omega_{ij}\Omega_{ij} - S_{ij}S_{ij}\right) = -\frac{1}{2}u_{i,j}u_{j,i} \tag{8}$$

where $\Omega_{ij} = \frac{1}{2}\left(u_{i,j} - u_{j,i}\right)$ and $S_{ij} = \frac{1}{2}\left(u_{i,j} + u_{j,i}\right)$ are the rotation rate and the strain rate, respectively. The invariant Q describes the balance between pure strain and fluid rotation. The surface of positive Q represents the region where the rotation overcomes strain in strength so that coherent vortex structures are effectively identified. In the figure, the iso-surfaces Q = 5000 [s^{-2}] are contoured by the vorticity in the cylinder axis (i.e., the local z axis) from -300 [s^{-1}] to 300 [s^{-1}]. The figure clearly visualizes vortex flow structures rotating along the cylinder axis and their rotating directions.

Figure 5(a) shows vortex flow structures around a yawed bare cylinder. As the yaw angle of the cylinder increases, the axial velocity of flow along the cylinder axis increases, and the difference between pressures at stagnation line and pressure at base line becomes smaller so that the intensities of Kármán vortices are reduced (Yeo and Jones, 2009). In contrast to vortex flow structures shed coherently over a cylinder normal to flow, vortex flow structures around a yawed cylinder are not shed parallel to the cylinder axis, and their axis lines are not linear. Their separation is delayed at locations where intense low pressure is generated by swirling flows. The swirling flows, induced by the combination of the mitigated Kármán vortices and axial flow along the cylinder axis, have strong vorticity with axial velocity near the cylinder, and develop alternately from the upper and the lower surfaces of the cylinder while moving downward along the cylinder at a constant speed. This speed is approximately 90 % of the axial velocity component ($U\sin\beta$) of the incoming flow velocity U (see Figure 1). These flows generate multiple, alternately developing swirling flow structures and the corresponding peak forces at spatial intervals of an order of 10D. Note that the spatial interval is 10D in the simulations using 10D cylinder length and peri-

odic spanwise boundary condition. The swirling flows play a key role not only in developing the complex, three-dimensional flow oblique to a cylinder, but also in generating low frequency force components in comparison to high frequency force components induced by Kármán vortices. The details are provided in the literature (e.g., Yeo and Jones, 2008, 2009).

According to the authors' proposed mechanism for large-amplitude vibration of stay cables induced by oblique wind, the mitigated Kármán vortex shedding is a necessary condition for the generation of swirling flows that are a low frequency excitation source because the swirling flows can be developed on the mitigated Kármán vortices (Yeo and Jones, 2009). Therefore, an aerodynamic approach to suppressing the vortex shedding using stakes could be an effective mitigation strategy of the low-frequency, large-amplitude cable vibrations induced by oblique wind. A strake pattern to disturb the force generation mechanism itself can also be successful.

For a yawed cylinder with strakes, the strakes considerably disturb the development of the vortex flow structures observed in a bare yawed cylinder. In a type A cylinder, vortex flow structures are generated differently at the upper and the lower sides of the cylinder. The strakes on the upper side are aligned against the flow path and disturb rolled-up shear layer flow along the oblique cylinder. But those on the lower side are aligned along the flow path and their disturbance of vortex shedding is relatively small. This develops an asymmetric time-averaged pressure distribution along the circumference and generates non-zero time-averaged forces in the across-flow direction (the y axis in Fig. 1). Well-developed swirling flow along the cylinder is not observed. In a type B cylinder, two cases were investigated (see Fig. 3). For type B-1 (symmetric alignment of axial strakes from stagnation line), vortex flow structures shed alternately from both sides of the cylinder. Delayed detachment of vortex flow structures from the cylinder is observed at two locations along the cylinder length, which suggests that two swirling flow structures de-

velop simultaneously (i.e., spatial interval of 5*D*). For type B-2 (asymmetric alignment of axial strakes from stagnation line), vortex flow structures develop alternately as type B-1, but their delayed detachment occurs at one location along the cylinder length. This means that the swirling flow structures develop at 10*D* distances along the cylinder. The results show that even strakes of the same type can have a different influence on the flow field around a cylinder, and that the flow field can be significantly affected by the strake alignment (see, e.g., Fig. 3). In a type C cylinder, the coherence of vortex flow structures around the cylinder is significantly broken, and the respective separation delays cannot be clearly seen. This indicates that the strakes largely suppress Kármán vortex shedding and effectively disturb development of the swirling flows.

3.2 *Aerodynamic forces*

Figure 6 shows spatio-temporal distributions of force coefficients on cylinders with and without strakes. The horizontal and vertical axes represent non-dimensional time ($t^* = Ut/D$) and non-dimensional position along the cylinder axis (z/D), where t is the time in dimension, and z is the distance from the upper end of the cylinder along the cylinder axis.

Non-dimensional force coefficients (C_x and C_y) in the local x and y axes are defined as

$$C_x = \frac{F_x}{\frac{1}{2}\rho U^2 A}, \qquad C_y = \frac{F_y}{\frac{1}{2}\rho U^2 A} \tag{9}$$

where F_x and F_y are forces on the cylinder in the x and y axes, ρ is the density of the air, and A is a horizontally projected area of the cylinder; the projected area of strakes on the cylinder was not taken into account in this study.

For a yawed bare cylinder, Figure 6(a) shows that a sequence of peak forces on the cylinder are coherent over a finite length (approximately 5*D*), have spatial intervals of 10*D*, and move downward along the cylinder at a fixed speed (i.e., approximately $0.9U\sin\beta$ as mentioned in the

previous section). The frequency of the moving peak forces is twice as high in the *x* axis (i.e., along the flow direction) than in the *y* axis (across the flow direction) (Yeo and Jones, 2008), which indicates that the swirling flow generating the moving peak forces is closely related to the von Kármán vortices. The sequence of moving peak forces due to swirling flow is the main aerodynamic behavior of a circular cylinder in oblique flow.

Flow-induced forces on a yawed cylinder with strakes are strongly influenced in time and space by their strake patterns (Figs. 6(b) to 6(e)). For the strake pattern of type A, a three-peak stationary pattern of forces is observed (Fig. 6b). The strakes significantly increase the drag force and the fluctuating lift force. The mean of the fluctuating lift force is non-zero.

For the strake pattern of type B, peak forces that move along the cylinder axis are observed, which means peak forces are generated as in the case of a bare cylinder. For type B-1 a clear pattern exhibiting two peak forces is generated along the 10*D* cylinder length, which moves downward along the cylinder axis. Although the spatial intervals of the peak forces are reduced from 10D to 5D due to the symmetrically aligned axial stakes, it is notable that the three-dimensional force generation is still valid in the type B-1 cylinder. In type B-2, the peak forces of the 10*D* spatial intervals move along the cylinder axis, but the patterns are not as clear as for type B-1 or for the bare cylinder.

For the strake pattern of type C, unlike for type A, no moving peak forces along the cylinder axis are observed. For type C the peak forces have much weaker fluctuations in both *x* and *y* axes than for type A, and the time-averaged lift force in the *y* axis is zero.

This study focuses on the investigation of strake patterns that mitigate wind-induced, large-amplitude and low-frequency vibrations of stay cables in cable-stayed bridges. Therefore, one question that needs to be addressed: how effectively can strakes disturb aerodynamic forces that

fluctuate at low frequencies and produce large-amplitude vibrations? The frequency distributions of forces (C_x and C_y) are shown in Figure 7 using the fast Fourier transform (FFT) to compute the power spectral density (PSD) of the corresponding force coefficients. The ordinate denotes the non-dimensional position of the cylinder along the cylinder axis (z/D), and the abscissa is the non-dimensional reduced frequency ($f_r = Df/U$), where f is the frequency of the force coefficients. The results show that the intensity of the force fluctuations is much larger in the y axis (i.e., across-flow direction) than in the x axis (along-flow direction), meaning that the flow-induced forces excite a yawed cylinder in the y axis. This result agrees well with field observations which show that wind-induced large amplitude vibrations of stay cables occur at low frequencies in the direction normal to the plane defined by the cable axis and the wind velocity vector (Zuo et al., 2008).

For a yawed bare cylinder (Fig. 7(a)), the forces acting along the y axis have discrete components with reduced frequencies distributed about the center of the mitigated Kármán vortex shedding frequency ($f_r = 0.191$) at $\Delta f_r = 0.059$ intervals. The intervals are the same for the reduced frequencies of the forces acting along the x axis. This coincidence is due to the modulation of the force amplitude and frequency (Yeo and Jones, 2009). Note that the power spectrum density (PSD) of C_y has the highest peak at $f_r = 0.132$, not at the vortex shedding frequency.

For a yawed cylinder with strakes (Figs. 7(b) to 7(e)), the effects of strake patterns on the frequency distribution of the forces are significant. In a type A cylinder, one peak frequency is shown at $f_r = 0.117$ for both x and y axes, and no low frequency component exists. In a type B cylinder, the frequency distributions of the forces are significantly different between type B-1 and type B-2. For type B-1, peak forces at 5D spatial intervals have peak frequency 0.138 for the y axis. For type B-2, peak forces of 10D spatial intervals have y-axis discrete frequencies at ap-

proximately constant intervals and have a peak at a low frequency of f_r = 0.085. The frequency distributions are similar to those of the yawed bare cylinder (Fig. 7(a)). The results confirm that the stake alignment with respect to the approaching flow significantly affects the aerodynamic forces, even in a cylinder with the same strake pattern. In a type C cylinder, the *y*-axis peak frequency is 0.167 and the *x*-axis peak frequencies are scattered, and frequency components are not discrete, as is the case for type A. Note that the PSD of C_y at the peak frequency is much lower than for the other strake patterns (Fig. 8), which means that type C stakes are the most effective of the strake patterns considered in this study.

The characteristics of forces due to the strake patterns are of importance from the designer's point of view for several reasons. Increased mean and fluctuating forces, while not related to large-amplitude, low-frequency vibrations, increase steady wind loads and cause fatigue, respectively. Therefore an appropriate strake pattern break 3-D flow structures generating the low-frequency components of the forces as well as reducing the strength of those forces. Figure 9 compares characteristics of flow-induced forces for various strake patterns. For strength purposes all cylinders used in the study have the same diameter (i.e., the same cross-section area). Strakes are attached to those cylinders. The aerodynamic forces on the bare cylinder are therefore clearly smaller than on the cylinders with strakes. As seen in Figure 9, the obstruction of the flow by the strakes substantially increases the drag force -- see also Naudascher and Rockwell (1994). This is a disadvantage of using strakes. However, Figure 9 shows that other aerodynamic features are significantly affected by strake patterns. The type A pattern has the largest time-averaged forces and fluctuations, and the type C pattern generates the smallest forces among cylinders with strakes investigated in this study.

The most effective strake is one that fully suppresses low-frequency moving forces and has the smallest time-averaged forces and fluctuations. Among the strake patterns investigated in this study, the type C strake pattern shows good performance in suppressing Kármán vortex shedding and therefore the three dimensional flow structures. However, further study is recommended for better understanding the true effectiveness of strake patterns, considering factors such as asymmetric alignment of strakes to flow direction, pitch, and shape of strakes.

4 CONCLUSIONS

Three-dimensional DES flow around a 40° yawed cylinder with various strake patterns was studied with a view to investigating their effectiveness in reducing large-amplitude, low-frequency vibrations of stay cables induced by oblique wind. Effects of the strake patterns on flow around, and the associated forces on, the cylinder were analyzed and compared to the aerodynamic characteristics of a yawed bare cylinder. Frequency distributions of the forces were examined to determine how the strake patterns effectively disturb or suppress the inherent mechanism of force generation along a cylinder oblique to flow.

Results showed that a suitable strake pattern causes disturbance of the development of coherent flow structures around an oblique cylinder. It consequently suppresses or weakens the associated forces at low frequency on the cylinder as a potential excitation source for the large-amplitude, low frequency vibrations. Because the flow-induced forces on an oblique bare cylinder develop by a modulation mechanism under mitigated von Kármán vortex flow structures, countermeasures that fully suppress von Kármán vortex flow structures are effective from an aerodynamics point of view.

Further investigations of the performance of strakes are required to find the optimal number, size, and pitch of the windings. The effectiveness of other types of surface modification, e.g., dimpled surfaces, should be investigated as well. In addition to ease of installation and maintenance, a practical aerodynamic instability control method should account for the aesthetic effect on cylindrical structures or cable structures such as cable-stayed bridges.

Appendix

In CWE (Computational Wind Engineering) research, two main procedures are used to assess the credibility of computational modeling and simulation: verification and validation (AIAA, 1998). In the verification process, the errors due to numerical modeling in a simulation are estimated and can be reduced. In a process of validation, the simulated results can be assessed in comparison to experimental data, and the flow characteristics in the simulations can be identified.

This research started with 2-D and 3-D simulations of flows normal to a circular cylinder at Reynolds number of 1.4×10^5. In DES, the flow region near a wall is treated in the RANS mode whose solution converges as the grid is refined. 2-D RANS, therefore, efficiently verifies the effects of two-dimensional grid refinements, timesteps, and numerical schemes on the simulated results. The verification associated with three-dimensional effects was performed in 3-D DES. The procedures are briefly summarized as follows, and further details are provided in Yeo (2008).

A.1 Verification Using a Cylinder Normal to Flow in 2-D RANS

For the verification of the numerical solution in 2-D RANS simulations, we investigated the effects of grid refinement (coarse, medium, and fine grids), the size of timestep (t^* = 0.005, 0.01,

and 0.04), the number of iterations per timestep in the Newton iterative method (2, 4, 8, and 16 iterations), and the order of the numerical scheme on the solution (2^{nd} and 5^{th}) on streamwise wind velocity along the centerline of the cylinder, pressure on the cylinder, and characteristics of forces on the cylinder (i.e., vortex shedding frequency, time-averaged drag force, and rms of lift force). Note that the medium grid used in the study (Fig. 4) is twice as fine as the coarse grid and is twice as coarse as the fine grid. The series of tests for verification provided what is considered to be the appropriate combination of numerical methods and parameters: the medium grid, the non-dimensional timestep of $t^* = 0.01$, 4 iterations per timestep in the Newton iterative method, and the 5^{th}-upwind scheme for convective terms.

A.2 Verification Using a Cylinder Normal to Flow in 3-D DES

We investigated spanwise numerical characteristics in 3-D DES: spanwise grid refinements ($\Delta z = D/3$, $D/6$, and $D/12$), spanwise aspect ratios of the cylinder ($L/D = 4$ and 10, where L is the cylinder length), and spanwise boundary conditions (periodic and slip condition).

Grid refinement in each direction affects the resolution of flow structures in a 3-D simulation. But 3-D DES used in this study is a non-zonal, hybrid method of LES and RANS, and the switching process depends on a turbulence length scale (Eq. (1)) that results from a local maximum grid size of a 3-D grid element and its distance from the wall. Because the spanwise grid size Δz in the 3-D DES has the largest size than the others in the region of boundary layer flow, the spanwise grids play an important role in determining the turbulence length scale in three-dimensional simulations of a turbulent flow. Note that the grids in x and y directions were based on the verification of in 2-D simulations.

Through the investigation of the sensitivity of vortex flow structures, pressure, and the associated force on the cylinder to the spanwise grid Δz, it was determined that the spanwise grid size

$\Delta z = D/6$ provided the most reliable simulation of the flow. This confirms that the DES has high sensitivity to spanwise grid spacing and that the grid refinement in DES does not always provide an improved result, in agreement with experimental data in literature (Breuer, 2000; Travin et al., 1999).

The effect of the spanwise aspect ratio (L/D; L is the cylinder length) and spanwise boundary condition on the simulated flow field was also investigated; 4D and 10D cylinders, and periodic and slip wall conditions were employed, respectively. Compared with the flow around a 4D cylinder, the flow around a 10D cylinder shows more effectively the three-dimensional characteristics of the flow structures along the cylinder length, such as vortex dislocation, For the sensitivity to spanwise boundary conditions the characteristics of the flow did not show major differences. Therefore, a 10D cylinder using either spanwise condition successfully predicts three-dimensional flow characteristics around the cylinder normal to the flow.

A.3 Comparison with Experimental Data

To improve the trustworthiness of the simulated flow it is important to assess the numerical results by comparison to available experimental data. Figure A.1 compares the pressure distributions of a circular cylinder in smooth and turbulent flows at sub-critical Reynolds numbers from numerical results (Hansen and Forsythe, 2003; Krishnan et al., 2006) and experimental data (Batham, 1973; Kwok, 1986). According to the experimental data in the figure, the effect of turbulent flow on the pressures on the surface in the sub-critical regime is significant; the peak negative pressure increases and the separation of the flow is delayed behind the cylinder. This phenomenon is similar to drag crisis (Simiu and Scanlan, 1996, see p. 158). Turbulent flow, therefore, exhibits different characteristics of pressure distribution from that of smooth flow at the same Reynolds number in the sub-critical regime.

Both of the present and previous DES studies (Hansen and Forsythe, 2003; Krishnan et al., 2006; Travin et al., 1999) show that pressure distributions from DES are similar to characteristics of pressure distributions in a turbulent flow in the sub-critical regime. It results from the inherent properties of DES; the upstream flow in DES has turbulent viscosity which leads to the delay of flow separation from the cylinder. The pressure distribution in the present study, therefore, is in good agreement with that of the turbulent flow at the same Reynolds number in the sub-critical regime.

Figure A.2 demonstrates the variation of drag coefficients in smooth and turbulent flows with respect to Reynolds numbers. It shows that turbulence plays an important role in decreasing the drag forces in the sub-critical regime, where drag coefficient on a smooth surface is known as around 1.2 in a smooth flow (Simiu and Scanlan, 1996, p. 161). According to experimental results (Batham, 1973; Bruun and Davies, 1975; Cheung and Melbourne, 1983; Kwok, 1986), however, a moderate level of longitudinal turbulence intensity T_u and a small turbulence length scale L_u/D significantly reduce drag force in the sub-critical regime. The longitudinal turbulence intensity measures the streamwise velocity fluctuations of a turbulent flow, and the turbulent integral scale is a measure of the average size of turbulent eddies of the flow corresponding to the characteristic length where the turbulent energy is concentrated. (For the mathematical expressions, see, e.g., Simiu and Scanlan, 1996, pp. 52-53.) The reduction of drag force is closely related to the effect of a turbulent boundary layer flow before separation. As shown in Figure A.2, the time-averaged drag coefficient in the 3-D DES of this study is in good agreement with experimental test results for smooth flow in the critical regime and for turbulent flow in the sub-critical regime with a moderate level of turbulence intensity and a small turbulence length scale.

Table A.1 summarizes the characteristics of force coefficients, peak reduced frequency f_r, base pressure C_{pb}, and separation angle θ_{spr} based on numerical simulations (Hansen and Forsythe, 2003; Krishnan et al., 2006; Travin et al., 1999) and experiments (Cheung and Melbourne, 1983; Kwok, 1986). It also confirms that the characteristics of the flow and associated forces in this study ($z = 10D$, periodic B.C.) are in good agreement with the experimental data.

A.4 Verification Using a Cylinder Oblique to Flow in 3-D DES

Flows oblique to a 30° yawed and 45° inclined circular cylinder were simulated using 3-D DES with a view to investigating the characteristics of flow and the forces on the cylinder induced by the flow. The inclination angle is defined as the angle between a vertically sloped cylinder and its horizontal axis. In other words, let the end of a cylinder at point A be shifted along the Y axis to a point, say A', in Figure 1; the inclination angle is then the angle between line AC and line A'C. The effects of spanwise grid discretization ($\Delta z = D/3$, $D/6$, and $D/12$), aspect ratio of a cylinder (L/D = 10, 20, and 30), and spanwise wall boundary condition (periodic and slip conditions) were examined to check the reliability of the numerical results.

The simulated flow field around the cylinder showed high sensitivity to spanwise grid sizes, just as in the case of flow normal to a cylinder. For flow oblique to the cylinder the spanwise grids $\Delta z = D/6$ provided the most reliable simulation results. Two boundary conditions (periodic and slip wall) at spanwise walls were examined for spanwise aspect ratios L/D = 10, 20, and 30. In the case of slip wall conditions, even the $30D$ cylinder showed that the flow field was significantly affected by the boundary conditions. In particular, the flow field behind the upper end of the cylinder was influenced most significantly. All cylinders with the periodic condition, regardless of the aspect ratio, showed reliable simulations without significant influence on the flow by

the boundaries. However, for the 30*D* cylinder the flow around the cylinder was less affected by the boundaries. It was also found that the 10*D* cylinder with periodic boundary conditions enables simulations to fully develop the three-dimensional flow past an oblique circular cylinder of infinite extent.

References

AIAA, 1998. Guide for the verification and validation of computational fluid dynamics simulations. AIAA-G-077-1998, American Institute of Aeronautics and Astronautics, Reston, Virginia.

Batham, J.P., 1973. Pressure distributions on circular cylinders at critical Reynolds numbers. Journal of Fluid Mechanics 57(02), 209-228.

Breuer, M., 2000. A challenging test case for large eddy simulation: high Reynolds number circular cylinder flow. International Journal of Heat and Fluid Flow 21(5), 648-654.

Bruun, H.H., Davies, P.O.A.L., 1975. An experimental investigation of the unsteady pressure forces on a circular cylinder in a turbulent cross flow. Journal of Sound and Vibration 40(4), 535-559.

Cheung, J.C.K., Melbourne, W.H., 1983. Turbulence effects on some aerodynamic parameters of a circular cylinder at supercritical numbers. Journal of Wind Engineering and Industrial Aerodynamics 14(1-3), 399-410.

Choi, H., Jeon, W.-P., Kim, J., 2008. Control of flow over a bluff body. Annual Review of Fluid Mechanics 40(1), 113-139.

Hansen, R., Forsythe, J., 2003. Large and detached eddy simulations of a circular cylinder using unstructured grids, in: Proceedings of the 41st Aerospace Sciences Meeting and Exhibit, Reno, Nevada, AIAA 2003-775.

Hanson, A.R., 1966. Vortex shedding from yawed cylinders. AIAA journal 4(4), 738-740.

Hikami, Y., Shiraishi, N., 1988. Rain-wind induced vibrations of cables stayed bridges. Journal of Wind Engineering and Industrial Aerodynamics 29(1-3), 409-418.

Hunt, J.C.R., Wray, A.A., Moin, P., 1988. Eddies, stream, and convergence zones in turbulent flows. Report CTR-S88, Center for Turbulence Research.

Kawamura, T., Hayashi, T., 1994. Computation of flow around a yawed circular cylinder. JSME International Journal Series B 37(2), 229-236.

King, R., 1977. Vortex-excited oscillations of yawed circular cylinders. Journal of Fluids Engineering 99, 495-502.

Kleissl, K., Georgakis, C.T. 2010. Shape modifications of bridge cables for aerodynamic vibration control,. the Fourth International Conference on Structural Engineering, Mechanics and Computation, Cape Town, South Africa.

Krishnan, V., Squires, K.D., Forsythe, J., 2006. Prediction of the flow around a circular cylinder at high Reynolds number, in: Proceedings of the 44th AIAA Aerospace Sciences Meeting and Exhibit, Reno, Nevada.

Kwok, K.C.S., 1986. Turbulence effect on flow around circular cylinder. Journal of Engineering Mechanics 112(11), 1181-1197.

Lam, K., Lin, Y.F., Zou, L., Liu, Y., 2010. Investigation of turbulent flow past a yawed wavy cylinder. Journal of Fluids and Structures 26(7-8), 1078-1097.

Lam, K., Wang, F.H., Li, J.Y., So, R.M.C., 2004. Experimental investigation of the mean and fluctuating forces of wavy (varicose) cylinders in a cross-flow. Journal of Fluids and Structures 19(3), 321-334.

Larose, G.L., Savage, M.G., Jakobsen, J.B., 2003. Wind tunnel experiments on an inclined and yawed circular cylinder in the critical Reynolds number range, in: Proceedings of the 11th International Conference on Wind Engineering, Lubbock, Texas, 1705-1712.

Lucor, D., Karniadakis, G., 2003. Effects of oblique inflow in vortex-induced vibrations. Flow, Turbulence and Combustion 71(1-4), 375-389.

Main, J.A., Jones, N.P., 1999. Full-scale measurements of stay cable vibration, in: Proceedings of the 10th International Conference on Wind Engineering, Copenhagen, Denmark, 963-970.

Matsumoto, M., 1998. Observed behavior of prototype cable vibration and its generation mechanism, in: Proceedings of the Advances in Bridge Aerodynamics, Balkema, Rotterdam, The Netherlands, 189-211.

Matsumoto, M., Daito, Y., Kanamura, T., Shigemura, Y., Sakuma, S., Ishizaki, H., 1998. Wind-induced vibration of cables of cable-stayed bridges. Journal of Wind Engineering and Industrial Aerodynamics 74-76, 1015-1027.
Matsumoto, M., Shiraishi, N., Kitazawa, M., Knisely, C., Shirato, H., Kim, Y., Tsujii, M., 1990. Aerodynamic behavior of inclined circular cylinders-cable aerodynamics. Journal of Wind Engineering and Industrial Aerodynamics 33(1-2), 63-72.
Matsumoto, M., Shiraishi, N., Shirato, H., 1992. Rain-wind induced vibration of cables of cable-stayed bridges. Journal of Wind Engineering and Industrial Aerodynamics 43(1-3), 2011-2022.
Miyata, T., Yamada, H., Hojo, T., 1994. Aerodynamic response of PE stay cables with pattern indented surface, in: Proceedings of the IABSE/FIP International Conference on Cables-Stayed and Suspension Bridges, Deauville, 515-522.
Naudascher, E., Rockwell, D., 1994. Flow-induced vibrations: an engineering guide. A.A. Balkema, Rotterdam.
Phelan, R.S., Sarkar, P.P., Mehta, K.C., 2006. Full-scale measurements to investigate rain-wind induced cable-stay vibration and its mitigation. Journal of Bridge Engineering 11(3), 293-304.
Pinto, A., Broglia, R., Mascio, A.D., Campana, E.F., Rocco, P., 2006. Numerical investigation of the unsteady flow at high Reynolds number over a marine riser with helical strakes. ASME Conference Proceedings 2006(47497), 587-595.
Pontaza, J.P., Menon, R.G., Chen, H.-C., 2009. Three-dimensional numerical simulations of flows past smooth and rough/bare and helically straked circular cylinders allowed to undergo two degree-of-freedom motions. Journal of Offshore Mechanics and Arctic Engineering 131(2), 021301-7.
Ramberg, S.E., 1983. The effects of yaw and finite length upon the vortex wakes of stationary and vibrating circular cylinders. Journal of Fluid Mechanics 128(1), 81-107.
Ruscheweyh, H., 1994. Vortex excited vibrations, in: Wind-Excited Vibrations of Structures, H. Sockel, ed., 51-84.
Shirakashi, M., Hasegawa, A., Wakiya, S., 1986. Effect of the secondary flow on Karman vortex shedding from a yawed cylinder. Bulletin of the JSME-Japan Society of Mechanical Engineers 29(250), 1124-1128.
Shur, M.L., Spalart, P.R., Strelets, M., Travin, A., 1999. Detached-eddy simulation of an airfoil at high angle of attack, in: Proceedings of the 4th International Symposium on Engineering Turbulence Modelling and Measurements, Corsica, 676-682.
Simiu, E., Scanlan, R.H., 1996. Wind effects on structures. John Wiley & Sons.
Spalart, P.R., 2000. Strategies for turbulence modelling and simulations. International Journal of Heat and Fluid Flow 21(3), 252-263.
Spalart, P.R., Allmaras, S.R., 1992. A one-equation turbulence model for aerodynamic flows, in: Proceedings of the 30th Aerospace Sciences Meeting and Exhibit, Reno, NV, 1-22.
Spalart, P.R., Jou, W.H., Strelets, M., Allmaras, S.R., 1997. Comments on the feasibility of LES for wings, and on a hybrid RANS/LES approach, in: Proceedings of the Advances in DNS/LES, 1st AFOSR International Conference on DNS/LES, Ruston, LA, 137-147.
Tournier, C., Py, B., 1978. The behavior of naturally oscillating three dimensional flow around a cylinder. Journal of Fluid Mechanics 85, 161-186.
Travin, A., Shur, M.L., Strelets, M., Spalart, P.R., 1999. Detached-eddy simulations past a circular cylinder. Flow, Turbulence and Combustion 63(1), 293-313.
Van Atta, C.W., 1968. Experiments on Vortex Shedding from Yawed Circular Cylinders. AIAA journal 6(4), 931-933.
Verwiebe, C., Ruscheweyh, H., 1998. Recent research results concerning the exciting mechanisms of rain-wind-induced vibrations. Journal of Wind Engineering and Industrial Aerodynamics 74-76, 1005-1013.
Wang, F.H., Jiang, G.D., Lam, K., 2004. A study of velocity fields in the near wake of a wavy (varicose) cylinder by LDA. Flow Measurement and Instrumentation 15(2), 105-110.
Weaver, W., 1961. Wind-induced vibrations in antenna members. ASCE Journal Engineering Mechanics Division 87(EM1), 141-165.
Wind-US. 2009. http://www.grc.nasa.gov/WWW/winddocs/.
Yeo, D., 2008. Numerical simulation of 3-D aerodynamic behavior of a yawed, inclined circular cylinder. Ph.D. thesis, University of Illinois at Urbana-Champaign, Urbana.
Yeo, D., Jones, N.P., 2008. Investigation on 3-D characteristics of flow around a yawed and inclined circular cylinder. Journal of Wind Engineering and Industrial Aerodynamics 96(10-11), 1947-1960.
Yeo, D., Jones, N.P., 2009. A mechanism for large amplitude, wind-induced vibrations of stay cables, in: Proceedings of the Eleventh Americas Conference on Wind Engineering, San Juan, Puerto Rico.
Zdravkovich, M.M., 1981. Review and classification of various aerodynamic and hydrodynamic means for suppressing vortex shedding. Journal of Wind Engineering and Industrial Aerodynamics 7(2), 145-189.
Zhao, M., Cheng, L., Zhou, T., 2009. Direct numerical simulation of three-dimensional flow past a yawed circular cylinder of infinite length. Journal of Fluids and Structures 25(5), 831-847.

Zou, L., Lin, Y.-f., 2009. Force reduction of flow around a sinusoidal wavy cylinder. Journal of Hydrodynamics, Ser. B 21(3), 308-315.
Zuo, D., Jones, N.P., 2006. Understanding the mechanism of rain-wind-induced vibrations in the context of dry cable vibrations observed in the field and in the wind tunnel, in: Proceedings of the Wind Induced Vibrations of Cable Stay Bridges Workshop, St. Louis, MO.
Zuo, D., Jones, N.P., Main, J.A., 2008. Field observation of vortex- and rain-wind-induced stay-cable vibrations in a three-dimensional environment. Journal of Wind Engineering and Industrial Aerodynamics 96(6-7), 1124-1133.

Table A.1 Summary of characteristics of the flow normal to a circular cylinder

Case	Avg. C_D	RMS C_D	RMS C_L	f_r	- C_{pb}	θ_{spr}
Z=4*D*, coarse ΔZ	0.70	0.70	0.51	0.281	0.90	111.1
Z=4*D*, medium ΔZ	0.69	0.69	0.42	0.275	0.88	109.1
Z=4*D*, fine ΔZ	0.59	0.59	0.13	0.301	0.72	105.9
Z=10*D*, periodic B.C.	0.65	0.65	0.34	0.271	0.81	109.8
Z=10*D*, slip B.C.	0.63	0.63	0.32	0.267	0.80	109.8
Travin et al. (1999)	0.57	-	0.07	0.300	0.65	106.0
Hansen and Forsythe (2003)	0.59	-	-	0.290	0.72	108.0
Krishnan et al. (2006)	0.60	-	0.11	0.280	0.69	106.4
Kwok (1986)	0.582	-	-	-	-	125.0
Cheung and Melbourne (1983)	-	-	-	0.19~0.27	-	-

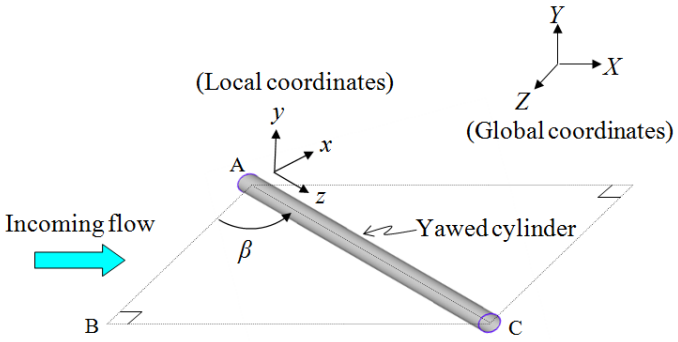

Figure 1. A yawed circular cylinder

(a) Type A

(b) Type B

(c) Type C

Figure 2. Strake patterns (cylinder length = 20*D*)

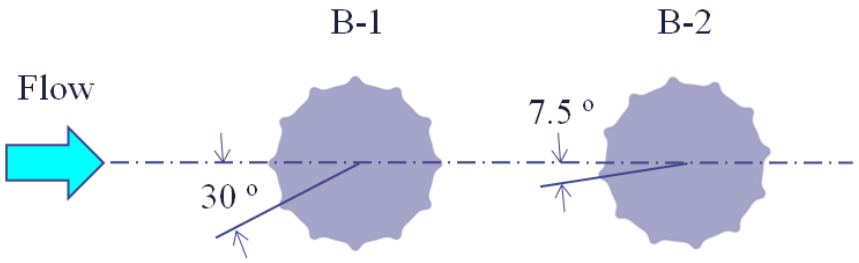

Figure 3. Strake alignment relative to flow direction (Type B)

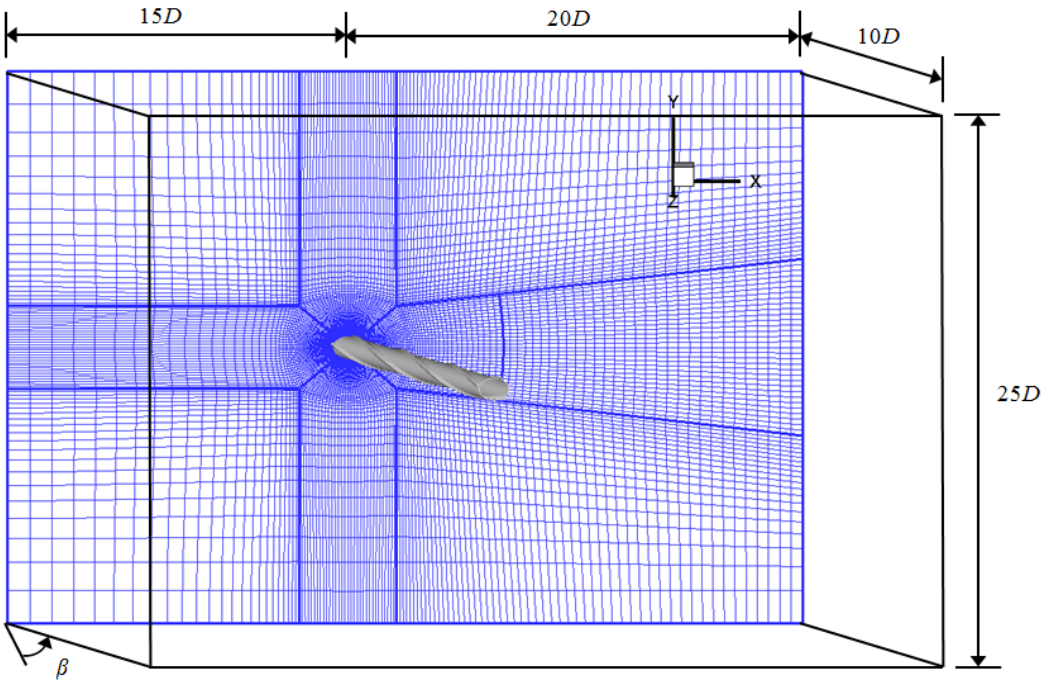

(a) Grids on the domain

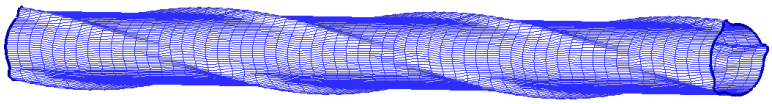

(b) Grids on the cylinder

Figure 4. Computational grids and domain

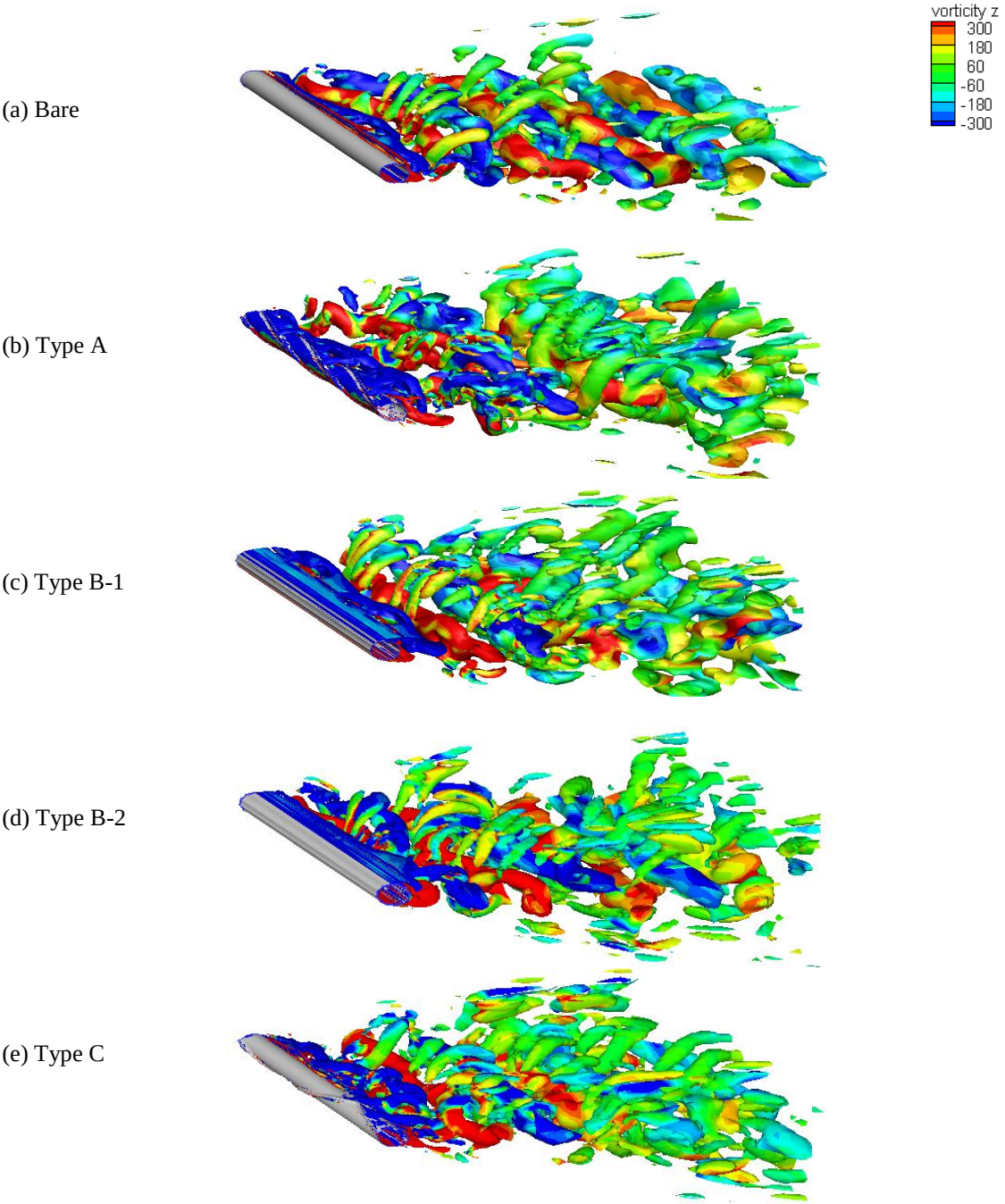

Figure 5. Vortex flow structures around a yawed cylinder

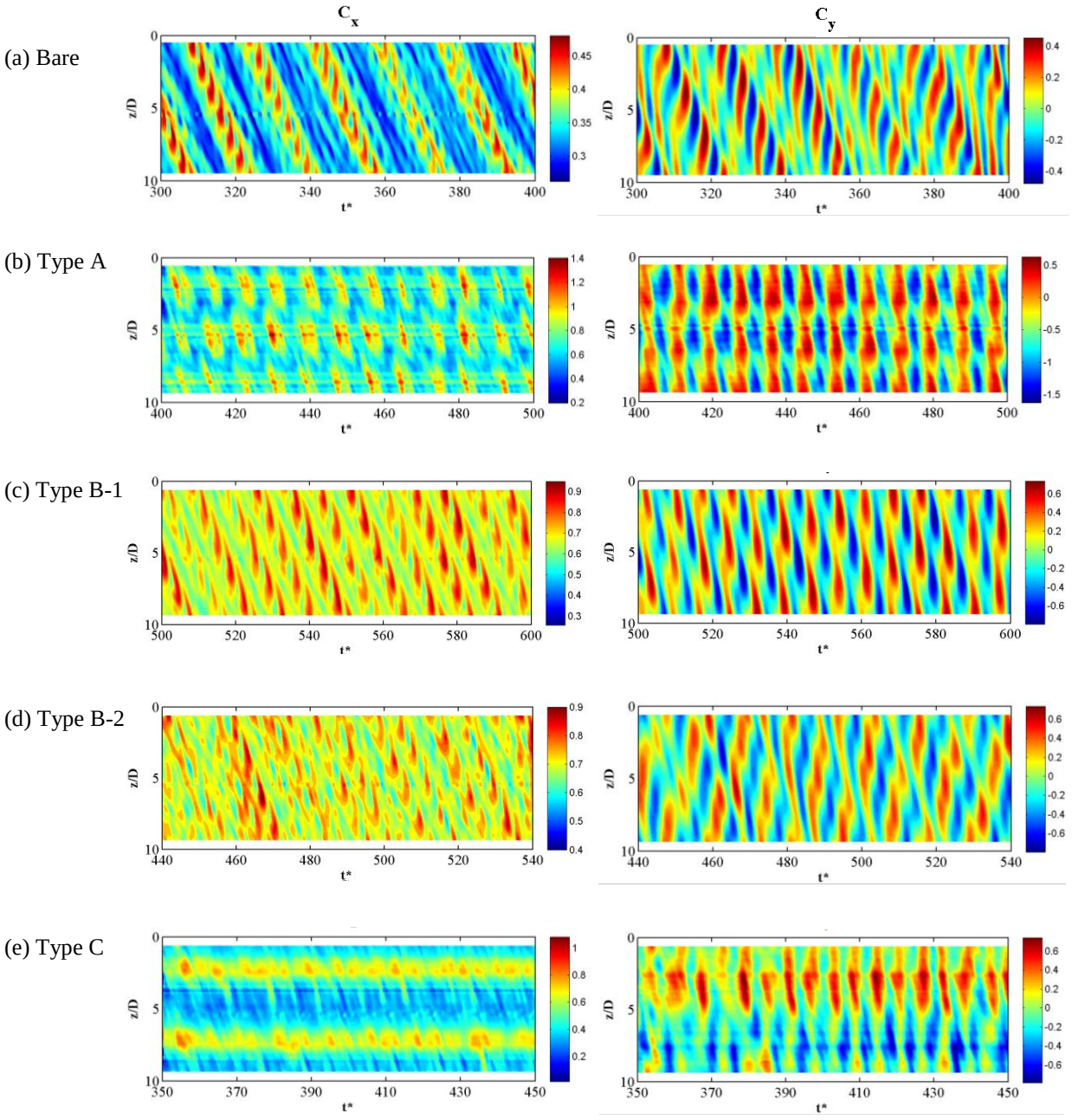

Figure 6. Spatial-temporal force distributions

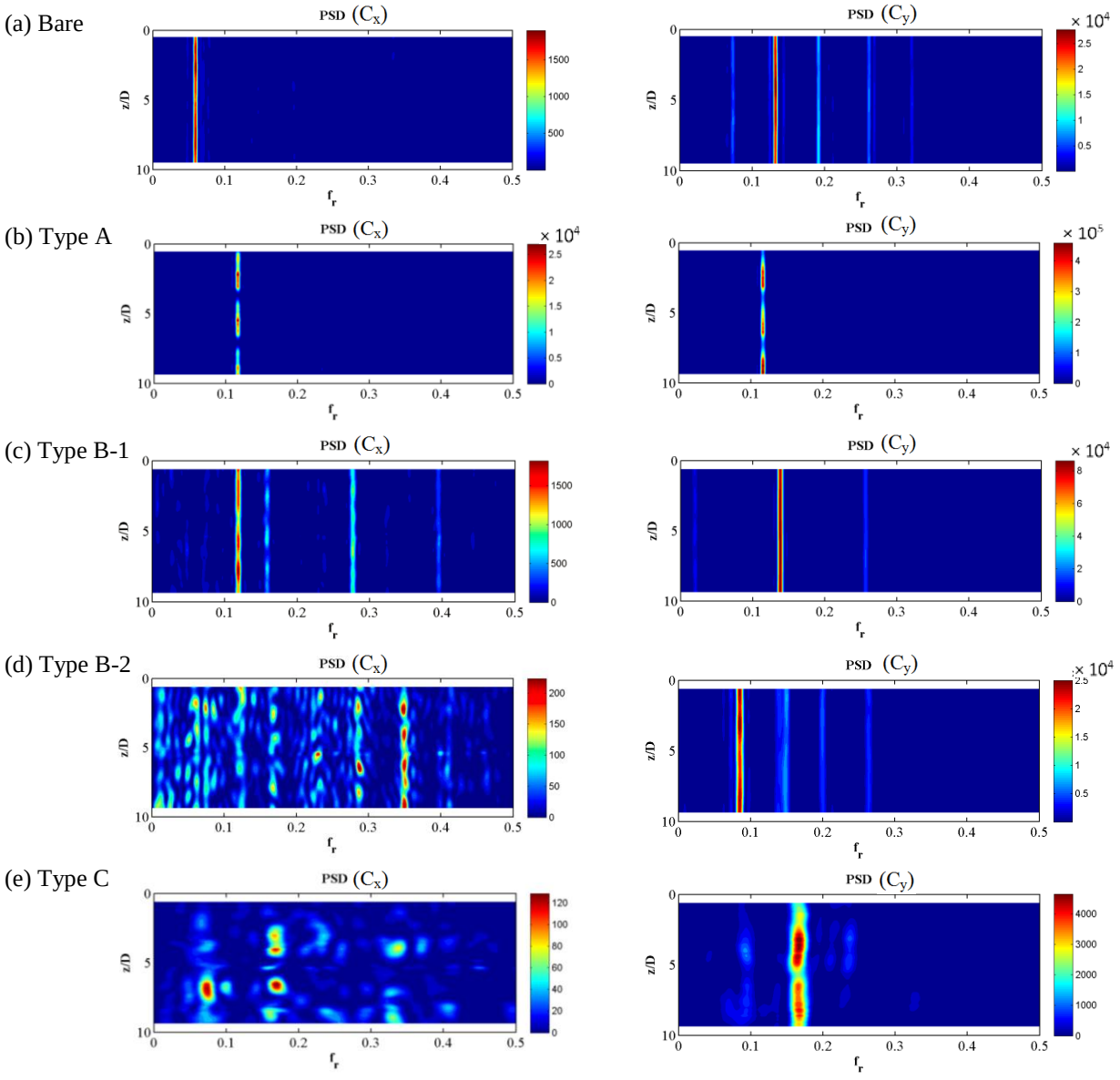

Figure 7. Frequency distribution of forces

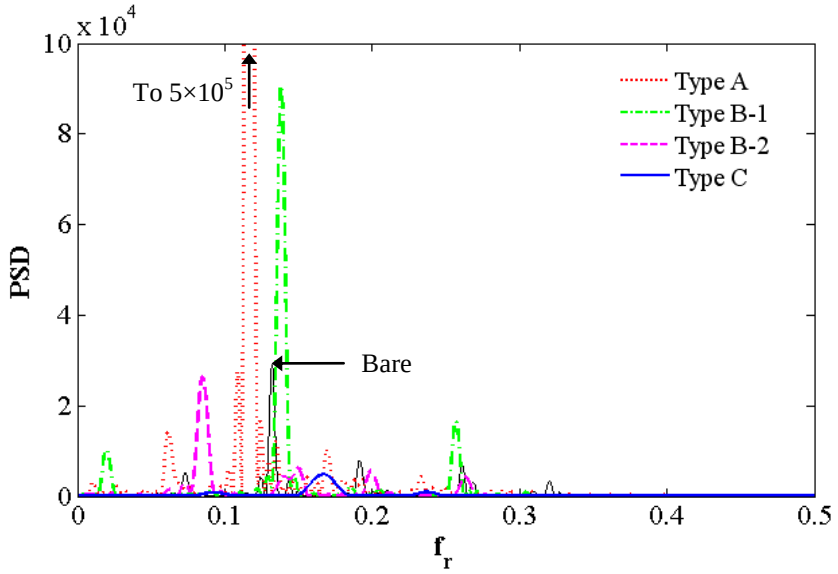

Figure 8. Power spectrum density of across-flow forces (C_y)

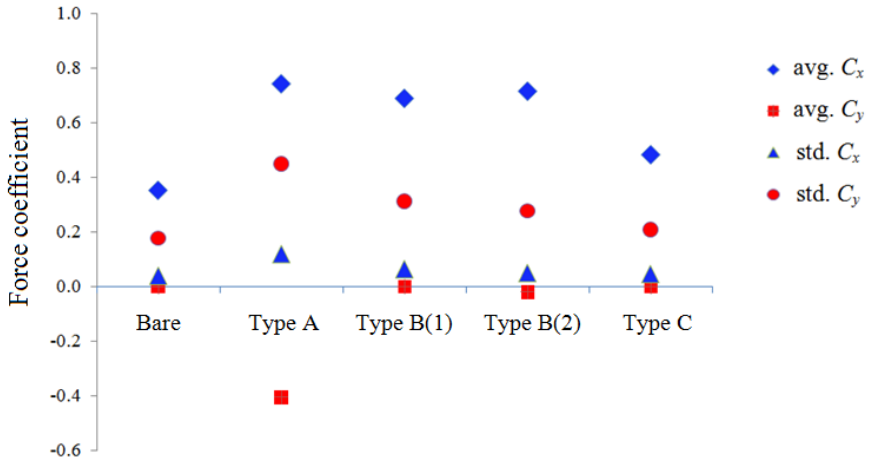

Figure 9. Characteristics of aerodynamic forces on a yawed cylinder

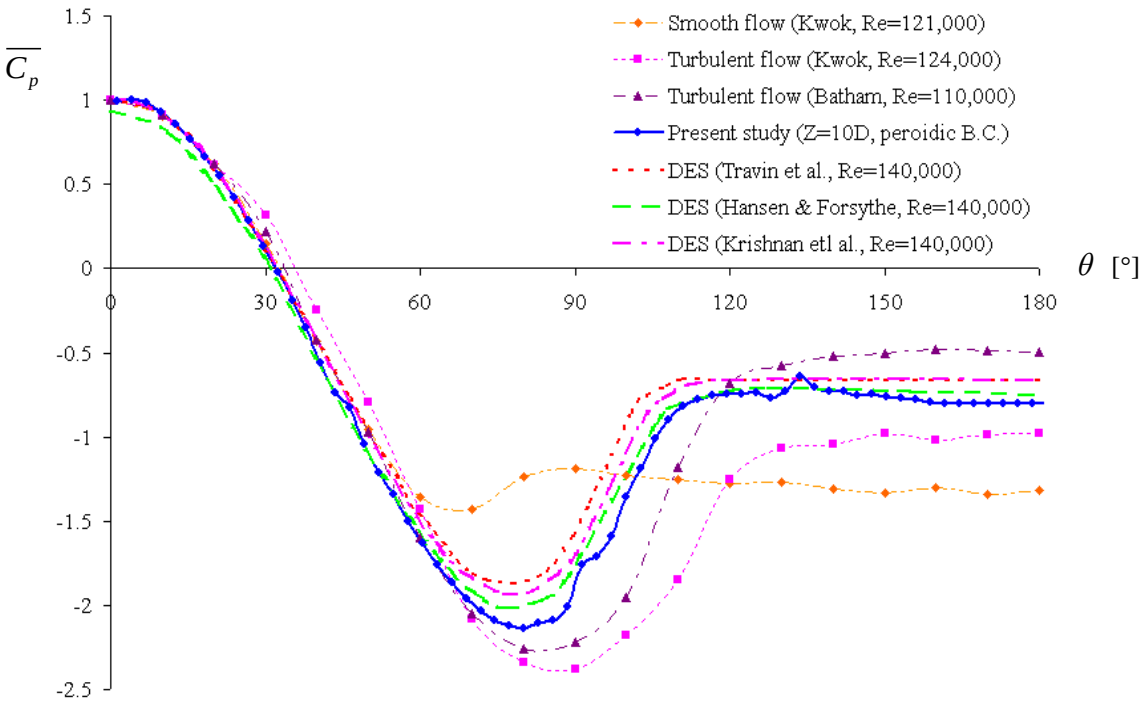

Figure A.1 Comparison of pressure coefficients

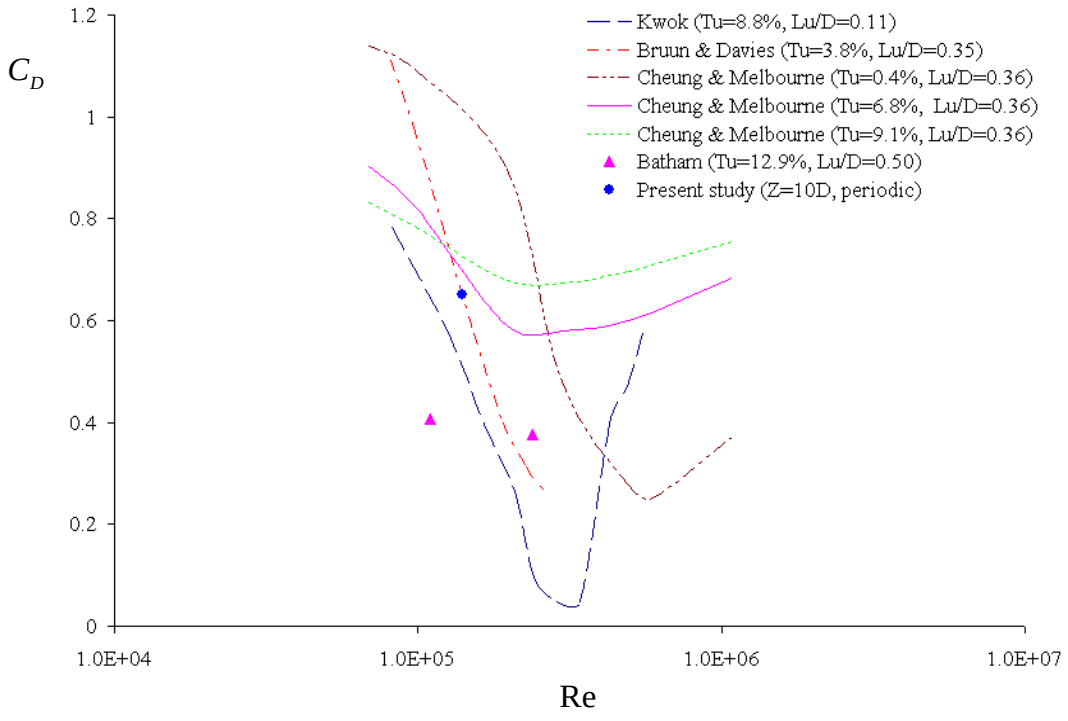

Figure A.2 Drag coefficients with Reynolds numbers